



Article

A Quantitative Multiparametric MRI Analysis Platform for Estimation of Robust Imaging Biomarkers in Clinical Oncology

Eve LoCastro ^{1,†}, Ramesh Paudyal ^{1,†}, Amaresha Shridhar Konar ¹, Peter S. LaViolette ², Oguz Akin ³, Vaios Hatzoglou ³, Alvin C. Goh ⁴, Bernard H. Bochner ⁴, Jonathan Rosenberg ⁵, Richard J. Wong ⁴, Nancy Y. Lee ⁶, Lawrence H. Schwartz ³ and Amita Shukla-Dave ^{1,3,*}

¹ Department of Medical Physics, Memorial Sloan Kettering Cancer Center, New York, NY 10065, USA; locastre@mskcc.org (E.L.); paudyalr@mskcc.org (R.P.); amareshks@gmail.com (A.S.K.)

² Department of Radiology, Medical College of Wisconsin, Milwaukee, WI 53226, USA; plaviole@mcw.edu

³ Department of Radiology, Memorial Sloan Kettering Cancer Center, New York, NY 10065, USA; akino@mskcc.org (O.A.); hatzogl@mskcc.org (V.H.); schwartzl@mskcc.org (L.H.S.)

⁴ Department of Surgery, Memorial Sloan Kettering Cancer Center, New York, NY 10065, USA; goha@mskcc.org (A.C.G.); bochnerb@mskcc.org (B.H.B.); wongr@mskcc.org (R.J.W.)

⁵ Department of Medicine, Memorial Sloan Kettering Cancer Center, New York, NY 10065, USA; rosenbj1@mskcc.org

⁶ Department of Radiation Oncology, Memorial Sloan Kettering Cancer Center, New York, NY 10065, USA; leen2@mskcc.org

* Correspondence: davea@mskcc.org; Tel.: +1-(212)-639-3184; Fax: +1-(212)-717-3010

† These authors contributed equally to this work.

Abstract: There is a need to develop user-friendly imaging tools estimating robust quantitative biomarkers (QIBs) from multiparametric (mp)MRI for clinical applications in oncology. Quantitative metrics derived from (mp)MRI can monitor and predict early responses to treatment, often prior to anatomical changes. We have developed a vendor-agnostic, flexible, and user-friendly MATLAB-based toolkit, MRI-Quantitative Analysis and Multiparametric Evaluation Routines (“MRI-QAMPER”, current release v3.0), for the estimation of quantitative metrics from dynamic contrast-enhanced (DCE) and multi-b value diffusion-weighted (DW) MR and MR relaxometry. MRI-QAMPER’s functionality includes generating numerical parametric maps from these methods reflecting tumor permeability, cellularity, and tissue morphology. MRI-QAMPER routines were validated using digital reference objects (DROs) for DCE and DW MRI, serving as initial approval stages in the National Cancer Institute Quantitative Imaging Network (NCI/QIN) software benchmark. MRI-QAMPER has participated in DCE and DW MRI Collaborative Challenge Projects (CCPs), which are key technical stages in the NCI/QIN benchmark. In a DCE CCP, QAMPER presented the best repeatability coefficient (RC = 0.56) across test–retest brain metastasis data, out of ten participating DCE software packages. In a DW CCP, QAMPER ranked among the top five (out of fourteen) tools with the highest area under the curve (AUC) for prostate cancer detection. This platform can seamlessly process mpMRI data from brain, head and neck, thyroid, prostate, pancreas, and bladder cancer. MRI-QAMPER prospectively analyzes dose de-escalation trial data for oropharyngeal cancer, which has earned it advanced NCI/QIN approval for expanded usage and applications in wider clinical trials.

Keywords: multiparametric MRI; dynamic contrast-enhanced MRI; diffusion-weighted MRI; optimal model mapping; cancer; oncology; quantitative imaging biomarkers



Citation: LoCastro, E.; Paudyal, R.; Konar, A.S.; LaViolette, P.S.; Akin, O.; Hatzoglou, V.; Goh, A.C.; Bochner, B.H.; Rosenberg, J.; Wong, R.J.; et al. A Quantitative Multiparametric MRI Analysis Platform for Estimation of Robust Imaging Biomarkers in Clinical Oncology. *Tomography* **2023**, *9*, 2052–2066. <https://doi.org/10.3390/tomography9060161>

Academic Editor: Emilio Quaia

Received: 14 September 2023

Revised: 12 October 2023

Accepted: 18 October 2023

Published: 3 November 2023



Copyright: © 2023 by the authors. Licensee MDPI, Basel, Switzerland. This article is an open access article distributed under the terms and conditions of the Creative Commons Attribution (CC BY) license (<https://creativecommons.org/licenses/by/4.0/>).

1. Introduction

Technical developments in MRI hardware and data acquisition have given us unique insights into the biology of normal tissue and complex diseases [1,2]. The acquired anatomic and physiological MR images can be used for qualitative evaluation [3,4] and quantitative

measurement of model-based imaging metrics from multiparametric (mp)MRI [5–7]. For example, quantitative imaging biomarkers (QIBs) derived from dynamic contrast-enhanced (DCE)-MRI, multi-b value diffusion-weighted (DW)-MRI, and MR relaxometry are surrogates of tumor perfusion, cellularity, and tissue morphology [8]. Furthermore, qualitative and quantitative analyses of mpMRI data have shown promise for tumor detection, assessment of treatment response, and outcomes in clinical oncology [4,7–10].

Some challenges to the clinical application of mpMRI include robust data acquisition, analysis techniques, and standardized guidelines for interpreting the results [11]. The limitations also include the limited availability of comprehensive mpMRI analysis tools and the reporting standards of the robustly derived QIBs [7,8]. For this purpose, the Quantitative Imaging Network (QIN) of the National Cancer Institute (NCI) has developed a five-level benchmark of criteria used to evaluate the performance and clinical readiness of aspiring software tools to provide QIB analysis for prospective clinical treatment and research [12]. The benchmarks range from initial testing against digital reference objects (DRO), participation in collaborative challenge projects (CCPs) with test–retest results, and demonstration of its usage in clinical trials [12]. Digital reference objects (DROs) are integral to developing and standardizing data analysis routines [13]. DROs offer a known ground truth and are artificially generated images designed to mimic acquired data [14]. The advantages of DROs include adding an explicit amount of random noise that distorts the generated signal, which tests an algorithm’s performance to see whether it can recover the known ground truth despite inconsistencies in image quality that are typically present in real-world images [7]. The scope of available QIN-approved tools spans multiple imaging modalities (CT, PET, and MRI) with a range of functionalities, including quality assurance tools, quantitative parametric mapping, and auto-segmentation routines [15]. Mature software tools in the QIN catalog must be proven to work consistently with DROs and CCPs.

Therefore, we have developed a vendor-agnostic, full-featured, and user-friendly MATLAB-based toolkit, Quantitative Analysis and Multiparametric Evaluation Routines for MRI (“MRI-QAMPER”, current release v3.0). QAMPER performs the extraction of robust QIBs from mpMRI data, and we have progressively worked to validate results through QIN software benchmarks [12]. QAMPER’s principal functionality is to generate parametric maps reflecting tumor permeability, cellularity, and tissue morphology. The mpMRI data from the brain [16], head and neck [17], thyroid [18,19], prostate [20], pancreas [21], and bladder (under review) have been seamlessly analyzed with QAMPER. Parametric maps obtained from quantitative mpMRI images can reveal spatial heterogeneity within tumors and provide numerical values for the underlying physiology.

Major MRI vendors have the capability to perform semi-quantitative DCE analysis and monoexponential DW modeling at the scanner. There are open-source resources with models for DCE and/or DW and/or MR relaxometry analysis [22,23]. QAMPER is a one-stop shop for converting and analyzing mpMRI, which can be directly implemented in MATLAB without the need for users to compile software binaries. When considering quantitative imaging metrics from DCE and DW MRI data, most studies apply a single data-fitting model to the whole tumor. However, no single model is sufficient to capture all the physiological characteristics of a tumor [24,25]. The optimal model mapping (OMM) method implemented in MRI-QAMPER for DCE [19] and DW MRI [25] performs voxel-wise analysis using multiple data fitting algorithms within tumor regions of interest based on a statistical approach. The OMM selection method serves to identify the best model to describe the data and to aid in depicting and understanding tumor heterogeneity.

In the Methods section of this article, we will explain in detail how we implemented our platform for mpMRI data analysis, from DICOM import and conversion to numerical parameter map generation and nested model selection. The Results section summarizes the NCI/QIN software benchmark validation steps explored through DRO and QIN CCP avenues.

2. Materials and Methods

MRI-QAMPER is currently available as a MATLAB-based toolkit (The Mathworks, Natick, MA, United States). The software imports DICOM images from major MRI vendors and different field-strength MRI scanners for post-processing of DCE MRI, multi-b-value DW MRI, T_1 mapping with multi-flip angle, and T_2 mapping with multi-echo MR relaxometry. It includes organ-specific presets and boundary conditions, allowing user-customized parameters for each non-linear fitting model of mpMRI data. MRI-QAMPER is approved by NCI/QIN and has currently earned Level 5 “Clinical Benchmark” status for use in clinical trials [12].

Figure 1 shows an overview of the MRI-QAMPER workflow. The graphical user interface offers an intuitive, step-by-step process to streamline analysis. The software is vendor-agnostic and will analyze mpMR images from the brain to the pelvis in clinical studies. It can be easily modified for other organs or preclinical data. QAMPER works natively with NIfTI image files [26] and includes an interface to convert DICOM images and import relevant image header acquisition metadata (i.e., flip angle (FA), repetition time (TR), number of phases, and b-values, as necessary). Regions of Interest (ROIs) label masks are saved in NIfTI imaging format in the same space and resolution as the MRI sequence for processing. Our group employs ITK-SNAP [27] to contour and save compatible NIfTI files for use with MRI-QAMPER, and to review result maps. Figure 2 is a schematic summary of the variety of models available for processing DCE, DW, T_1 , and T_2 MRI data. QAMPER’s analyses range from commonly available data fitting routines [28] to more advanced data modeling algorithms [5,24,25,29,30] and MR relaxometry analysis methods, which are detailed as follows.

2.1. DCE MRI Pharmacokinetic Modeling

DCE MRI time course analysis focuses on extravasation and transport of contrast agent (CA) in tissue, particularly their distribution within and elimination from the body [9]. T_1 -weighted DCE imaging involves a series of data acquisition before, during, and after intravenous injection of a Gadolinium-based CA [28]. T_1 mapping is performed with multiple FAs for the estimation of pre-contrast T_1 (ie, T_{10}) [31,32] needed for Equation (1). The spoiled gradient recalled (SPGR) acquisition Equation used for T_{10} fitting is provided in Appendix A (Equation (A2)).

The change in water proton relaxation rate (i.e., $\Delta R_1(t) = (R_1(t) - R_{10}) [s^{-1}]$) due to CA relaxivity, $r_1 [(mM)^{-1}s^{-1}]$, is linearly related to the tissue CA concentration, $C_t (mM)$,

$$R_1(t) = R_{10} + r_1 C_t(t) \rightarrow \Delta R_1(t) = r_1 C_t(t), \quad (1)$$

where R_{10} is the pre-contrast longitudinal relaxation rate.

The signal in the DCE images is converted to tissue CA concentration via longitudinal T_1 -relaxation [31], requiring measurement of the pre-contrast R_{10} ($=1/T_{10}$) and arterial input function (AIF) from the major artery within the field of view (FOV). DCE pharmacokinetic analysis can be performed to estimate physiological parameters via compartmental models ranging from complex to simple, providing plasma (blood) flow (F_p), permeability surface area product (PS), volume fractions of blood plasma (v_p), and extracellular extravascular space (EES) (v_e).

Figure 2 shows the various DCE pharmacokinetic models that can be used to analyze data where the application of the optimal model selection depends on tumor heterogeneity. The most general two-compartment exchange model (2CXM: F_p , PS, v_e , and v_p) [5] reduces to nested simpler models under special approximation, including the compartmental tissue uptake model (CTUM F_p , PS, and v_p) [5], extended Tofts model (ETM: K^{trans} , v_e , and v_p) [28], Tofts Model (TM: K^{trans} and v_e) [28], and Patlak model (PM: K^{trans} and v_p) [33]. These models assume an infinitely fast water exchange between the tissue compartments, called fast water exchange limit (FXL). On the other hand, the shutter speed model (SSM) model (also referred to as fast exchange regime (FXR)) describes the finite rate of water exchange across the cell membrane between intracellular space (ICS) and EES [34], providing estimates of the mean lifetime of the water molecule in intracellular space (τ_i) in addition to K^{trans} and v_e . The

comprehensive list of DCE MRI routines available in QAMPER includes 2CXM, CTUM, ETM, TM, PM, and SSM (Figure 2). Herein, we describe the commonly used Tofts models.

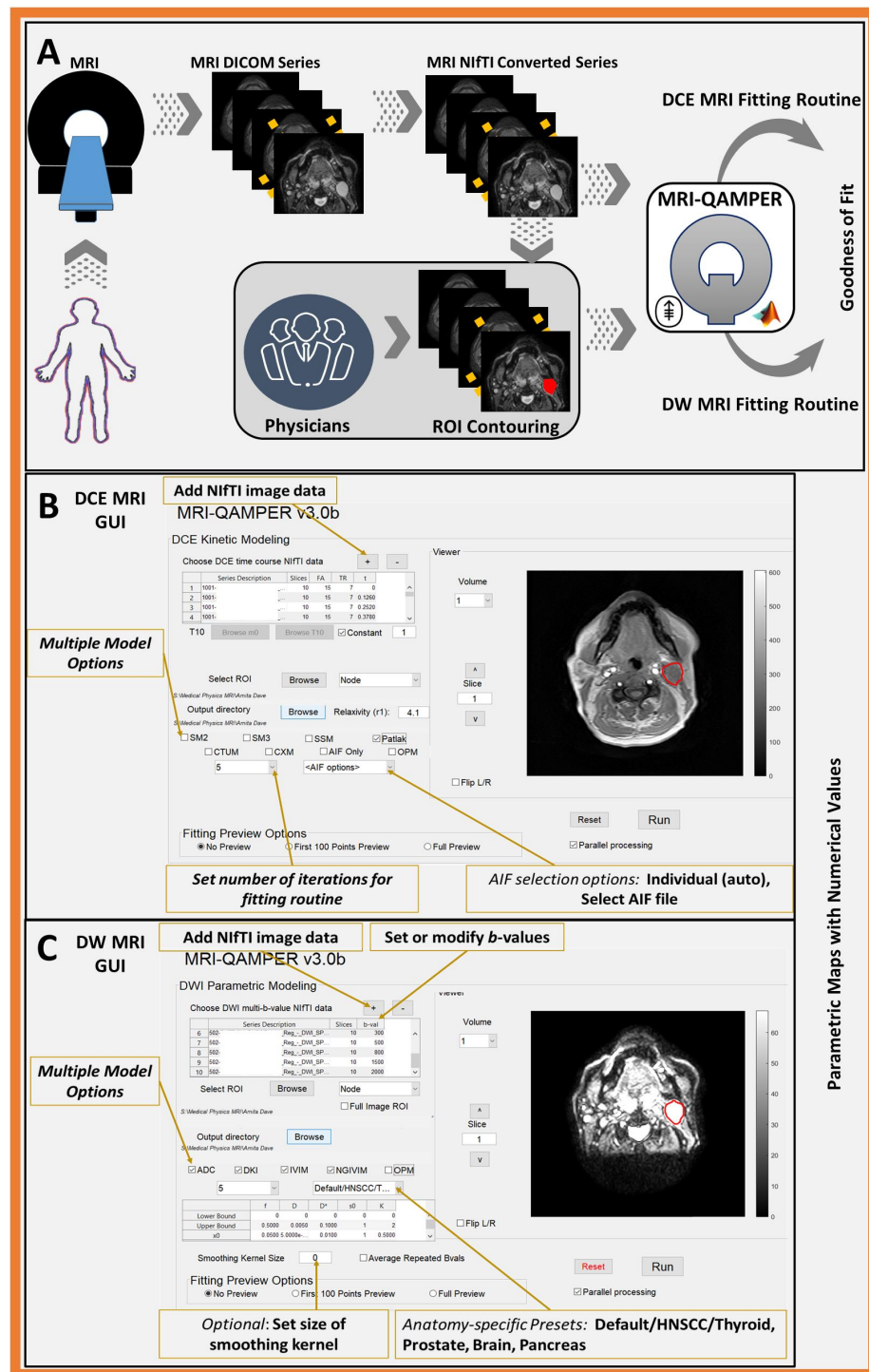


Figure 1. Workflow of MRI-QAMPER v3.0: (A) Images are acquired from MRI scanner and converted from DICOM to NIFTI. Skilled physician or planner contours ROI on image. The NIFTI MR images and ROI are loaded into the MRI-QAMPER GUI. (B) View of the MRI-QAMPER DCE GUI, with preview of patient image with ROI overlaid. Interface provides options for selecting multiple DCE routine for analysis, parameter bounds, option for OMM and AIF. (C) View of the MRI-QAMPER DW GUI, with patient and ROI preview. Interface provides options for selecting multiple DW routines, parameter bounds, manual toggling/editing of b-values and OMM option.

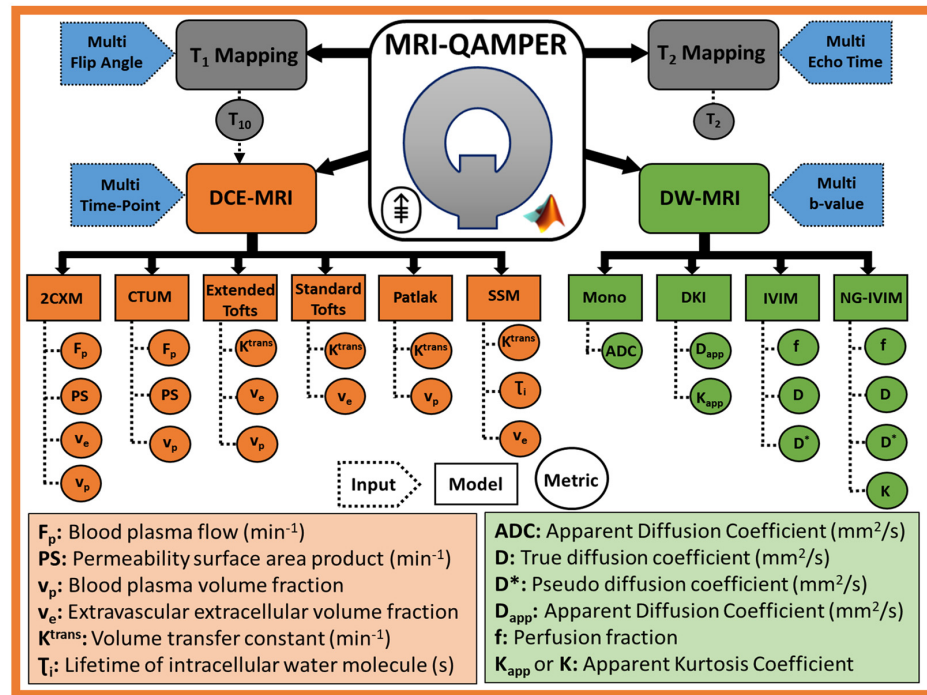


Figure 2. Schematic of image processing routines included with MRI-QAMPER v3.0. The software provides methods for: multi-flip angle T_1 mapping, multi-echo T_2 relaxometry, multi-compartmental methods for DCE, and fitting for multi-b-value DW imaging.

2.1.1. Extended Tofts Model (ETM)

ETM assumes a two-compartment model (vascular space and EES) expression for modeling $C_t(t)$ is given by Equation (2), and standard TM is obtained assuming a weakly vascularized ($v_p \rightarrow 0$) (Equation (3)).

$$C_t(t) = K^{\text{trans}} e^{-k_{ep}} \otimes C_p(t) + v_p C_p(t) \tag{2}$$

$$C_t(t) = K^{\text{trans}} e^{-k_{ep}} \otimes C_p(t) \tag{3}$$

where the \otimes operator denotes the convolution function. C_p and C_t are the plasma space and tissue CA concentrations, respectively. k_{ep} is the backward flux from the EES to vascular space.

2.1.2. Patlak Model (PM)

The two-parameter Patlak model ignores back flux to the vascular space from EES. The extended Patlak model is equivalent to the ETM [33].

$$C_t(t) = K^{\text{trans}} \otimes C_p(t) + v_p C_p(t) \tag{4}$$

2.1.3. Fast Exchange Regime (FXR) or Shutter Speed Model (SSM)

In biological tissue, water protons reside in three compartments: intravascular space, EES, and ICS [35]. Equilibrium water exchange kinetics occur between these compartments. Two- and three-site two-water exchange models have been developed to account for the water exchange kinetics in estimates of T_1 relaxation [36]. FXR is a two-compartment model that accounts for equilibrium water exchange across cell membranes between intracellular space and EES [34]. FXR is formulated in Equation (5), in terms of nonlinear R_1 ($\equiv 1/T_1$), incorporating EES CA concentration ($C_e(t) = C_t(t)/v_e$) from Equation (3) into

Equation (5), rather than using the linear relationship between the change in R_1 (ΔR_1) with C_t (Equation (1)). The equation for FXR is given by

$$R_{1f}(t) = \frac{1}{2} \left[(R_{1i} + k_{ie} + R_{10e} + r_1 C_e(t) + k_{ei}) - \sqrt{(R_{1i} + k_{ie} - R_{10e} - r_1 C_e(t) - k_{ei})^2 + 4 k_{ie} k_{ei}} \right] \quad (5)$$

where R_{1i} and R_{10e} are pre-contrast R_1 for ICS and EES; k_{ie} in the inverse of mean lifetime of intracellular water protons, $\tau_i=1/k_{ie}$; and k_{ei} is the rate of water exchange from ICS to EES (vice versa for k_{ei}).

Detailed equations for signal-to-CA conversion, CTUM, and 2CXM models are provided in the Appendix A.

2.1.4. Arterial Input Function (AIF) Selection

QAMPER provides options to perform DCE analysis using an AIF of the user's choice. This may be a curated or population-based AIF [37] or extraction of an individual-based AIF using QAMPER's automated method. Automated AIF detection is performed by identifying the major artery in the image field of view using time-wise cross-correlation analysis against an idealized reference function for each voxel in the DCE volume [38]. The contrast-enhanced image signal intensity curve is converted to $C_p(t)$ [31], which can then be used as the impulse function for compartmental DCE models.

2.2. DW MRI Data Modeling

Quantitative DW MRI measures the Brownian motion of water molecules at a cellular level. Multi-b-value acquisitions at low b-values ($b \leq 0-100$ s/mm²) and intermediate to high b-values ($b \geq 100-2000$ s/mm²) exhibit two distinct curvature signals. The standard monoexponential model calculates the apparent diffusion coefficient (ADC, Equation (6)), reflecting tumor cellularity, from imaging with at least ≥ 2 b-values using a straightforward linear regression fitting [39]. ADC is a composite metric accounting for molecular diffusion and microcapillary perfusion. LeBihan formulated a biexponential model (intravoxel incoherent motion (IVIM)), fitting multi-b-value signal with estimated metrics of the capillary network, i.e., pseudo-diffusion coefficient (D^*), perfusion fraction (f), and tissue true diffusion coefficient (D) (Equation (8)) [29]. IVIM estimation of f provides insight into vascular dynamics without CA injection. ADC and IVIM models assume a Gaussian probability distribution function for the displacement of the water molecules. The presence of underlying tissue microstructures in a tumor can alter the distribution of water diffusion from Gaussian to non-Gaussian (NG). Diffusion kurtosis imaging (DKI) (Equation (7)) was introduced to capture NG effects by expanding the DW signal to second-order higher b-values [30], represented by apparent kurtosis coefficient (K_{app}), a surrogate QIB of tissue microstructure, in addition to the apparent diffusion coefficient (D_{app}). NG-IVIM describes simultaneous perfusion and restricted diffusion by incorporating microstructure, K , the signal deviation from Gaussianity [25,29], providing estimates of the f , D^* , D , and K . Figure 2 shows QAMPER's available DW models, which can be used to analyze data and to identify the optimal model based on tumor heterogeneity. The DW MRI model equations are as follows:

2.2.1. Monoexponential model [39]:

$$S_b = S_0 e^{-b \times \text{ADC}} \quad (6)$$

where S_b and S_0 are signal intensities with and without diffusion-weighting factor b (s/mm²), respectively.

2.2.2. DKI model [30]:

$$S = S_0 e^{-b \times D_{app} + \frac{1}{6} K_{app} (b \times D_{app})^2} \quad (7)$$

2.2.3. Intravoxel incoherent motion (IVIM) model [29]:

$$S = S_0(fe^{-b \times D^*}) + (1 - f)e^{-b \times D} \quad (8)$$

2.2.4 Non-Gaussian intravoxel incoherent motion (NG-IVIM) model [25]:

$$S = S_0 (fe^{-b \times D^*}) + (1 - f)e^{-b \times D + \frac{1}{6}K(b \times D)^2} \quad (9)$$

2.3. T_1 and T_2 Relaxometry

T_1 and T_2 relaxometry measurements assess the water content fraction and vascular morphology through multiple acquisitions of varying imaging parameters [40]. For quantification of T_1 and T_2 values, the standard approaches are inversion recovery (IR) with different inversion time (TI) values and multiple single spin-echo (SE) methods with varying echo time (TE) values. Various methods have been developed to quantify T_1 and T_2 metric values within a clinically feasible timeframe [32,41–43]. Multi-echo T_2 mapping [44] can be tailored appropriately for different anatomical regions and physiological conditions.

Variable flip angle T_1 measurement allows T_1 value estimation in a clinically feasible time using multiple spoiled gradient echo acquisitions with different FA [32]. The Equation is given in Appendix A (A2).

A multi-echo spin-echo sequence is commonly used for T_2 mapping, and the Equation is given by [44].

$$S = S_0 e^{-\frac{TE}{T_2}} \quad (10)$$

where TE is the echo time.

2.4. Optimal Model Mapping (OMM)

Model selection techniques for DCE or DW MRI data fitting refer to identifying the best model that more closely fits the data set for each voxel [24,25,31,45]. Heterogeneity within solid tumors and surrounding tissue, irregular levels of vasculature development, and leakiness are represented by different compartment models. The data acquisition methods and underlying tumor physiology need to be considered while applying OMM. The F-Statistic (F-test) [46], R-square (R^2) [31], chi-square (χ^2) [47], corrected Akaike information criteria (AICc) [19,48–50], and Bayesian information criteria (BIC) [25,51] have been used to select the model that most accurately reflects the tumor physiology and can be used to quantify values of imaging biomarkers in each voxel.

2.5. Imaging Formats and Conversion

QAMPER utilizes the dcm2nix conversion application to import DICOM images into NIfTI format for processing. The software readily accepts NIfTI images of ROI masks in matching coordinate space to the parent image, and generated parametric maps are output as NIfTI files. The output mapping data are simultaneously saved as MATLAB struct arrays in MAT files, plus additional metrics to assess the quality of fitted output: AIC [48], BIC [51], and R^2 . In addition to MATLAB, two open-source external dependencies are currently required to run MRI-QAMPER: dcm2nix [26] and NIfTI Toolbox for MATLAB.

3. Results

At our center, QAMPER has been used to analyze mpMRI data, which resulted in peer-reviewed articles on outcomes in various organs, such as the brain [16], head and neck [17], thyroid [18,19], prostate [20], pancreas [21], and bladder (article under review) (Figure 3). The software was evaluated using DROs and participated in CCPs and in clinical trials.

3.1. QAMPER QIN Software Validation: DROs and CCPs

The initial performance of the MRI-QAMPER routines was validated using well-established digital reference objects (DROs) for DCE and DW MRI, serving as early approval stages in the QIN software benchmark [12]. MRI-QAMPER has participated in DCE and DW QIN CCPs: (i) MR Relaxometry Brain OSUPI DCE Challenge (in press) led by Dr. Anahita Fathi Kazerooni (UPENN and CHOP) and (ii) Multi b-Value Prostate Challenge [20] led by Dr. Peter S. LaViolette (MCW). The software is approved for clinical trials and is routinely used for mpMRI data analysis in an oropharyngeal cancer dose de-escalation clinical trial (#NCT03323463) at MSKCC [10].

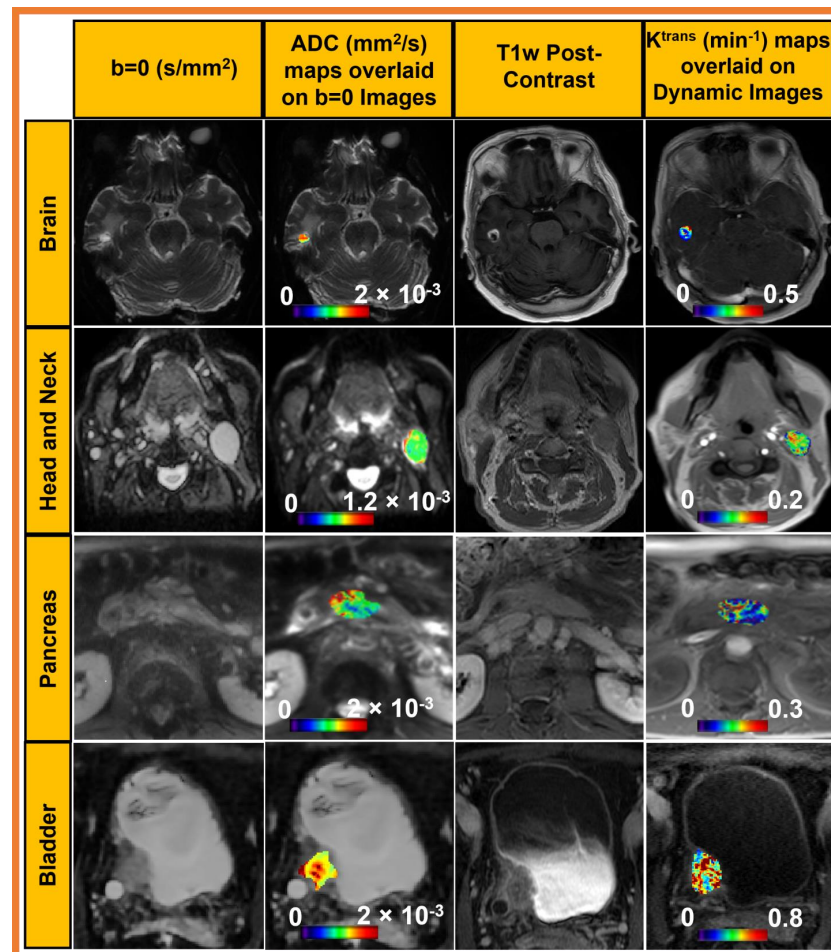


Figure 3. Representative output of MRI-QAMPER v3.0: input images (DW $b = 0$, T_1 -weighted base image) and output quantitative parametric maps (ADC, K^{trans}), computed for images in brain, head and neck, pancreas and bladder. Visualization of parametric map overlay was created with MRICron (v1.0.20190902) software.

3.2. DCE MRI DRO (RSNA)

QAMPER DCE perfusion routines were tested using the DCE DRO from the Radiological Society of North America (RSNA) Quantitative Imaging Biomarkers Alliance (QIBA; noise-free, three-parameter, extended, <https://sites.duke.edu/dblab/qibacontent/>, accessed on 10 October 2023) [52], developed in the Barboriak Lab, Duke University [14]. The ETM, three-parameter fit, model was used to fit a synthetic data slice with 661 time points. The resulting K^{trans} map from QAMPER showed excellent agreement with the ground truth.

3.3. DW MRI DRO (University of Michigan)

The diffusion DW MRI DRO developed by the Chenevert Lab, University of Michigan, was used to evaluate the performance of QAMPER routines for ADC, IVIM, and DKI [53]. This set of DROs was generated for advanced DW MRI clinical trial protocols. The generated DROs include simulated acquisition noise, DICOM scaling, and clinically relevant DW MRI parameter ranges for perfusion-fraction IVIM and DKI models. The resulting DW MRI-derived parametric maps showed excellent agreement with the ground truth.

3.4. Collaborative Challenge Projects

3.4.1. DCE CCP (ISMRM, Open Science Initiative for Perfusion Imaging (OSIPI))

The OSIPI Task Force on DCE/DSC challenges was formed to benchmark perfusion quantification methods by route of organized community challenges (in press) to craft a systematic and controlled framework to benchmark and progress K^{trans} calculation as a biomarker in brain tumors. This study reports results from the OSIPI-DCE challenge and highlights the high inter-software variability within K^{trans} estimation. The OSIPI-DCE challenge assessed the performance of 10 participating software packages according to their ability to accurately calculate K^{trans} from a set of generated synthetic data, repeatability of parameter calculation in test–retest scans of eight patients with glioblastoma, and reproducibility of the software from independent re-analysis of the data. QAMPER finished in the top four software packages out of ten at recapturing K^{trans} values from the synthetic data. QAMPER presented the best repeatability coefficient across the test–retest data among all packages tested, with RC = 0.56.

3.4.2. DW MRI CCP (QIN, MCW, Prostate)

A collaborative group organized by the NCI coordinated a multi-institutional study to explore how differences in DW fitting algorithms affect prostate cancer detection and how varying post-processing parameters differentiate regions of tumors by severity [20]. Results from 14 groups and software were verified against ground truth histological maps and pathologist-traced MRI annotations. The study aimed to measure the consistency of values in calculated metrics between sites and evaluate inter-site variability in performing a diagnostic task. Mono-exponential and kurtosis analyses were the most stable, presenting a low percent difference and high correlation coefficient, independent of site pairing permutations. The DW MRI study found that conventional diffusion models consistently differentiated prostate cancer from benign tissue. The results also indicated that post-processing decisions on DW MRI data could affect sensitivity and specificity when applied to radiological–pathological studies in prostate cancer. The parameters K, diffusion kurtosis (D_K), and ADC showed the least percent difference among sites and the highest correlation. QAMPER's ability to customize and set lower- and upper-threshold bounds was a feature that grouped it among the top five out of fourteen tools with the highest area under the curve (AUC) for prostate cancer detection [20].

3.5. DCE and DW MRI in Clinical Trial (Oropharyngeal Cancer)

At our center, MRI-QAMPER is routinely used to analyze mpMRI data obtained from oropharyngeal cancer patients enrolled in the dose de-escalation clinical trial (#NCT03323463) [10]. Pretreatment DCE MRI analyses confirmed a difference in perfusion and permeability between patients with residual disease and those with pathological complete response (pCR). In addition, in a small pilot study, DW MRI revealed changes in the ADC and relative K that were statistically significantly correlated with pCR at the time of surgery [10].

4. Discussion

Our in-house MATLAB toolbox was developed for the estimation of robust QIBs from mpMRI. DCE and DW MRI results obtained from MRI-QAMPER routines have been featured in numerous peer-reviewed publications [8,17,19,54]. The core software development has been supported by NIH funding and extended into an easily installable

MATLAB package with a graphical interface and capability for conversion of DICOM files and extraction of imaging metadata. MRI-QAMPER's ability to extract timing information from DCE MRI and b-values from DW MRI allows it to operate on MR images independent of the scanner vendor. The bounds for nonlinear fitting parameters can be user-set to be appropriate on a case-by-case basis, ensuring that results are physiologically relevant. The analysis routines are organ-independent due to the customizable parameters available in the MRI-QAMPER software and include several literature-based presets.

In oncological imaging, there is a need for proven quantitative imaging tools and the development of MRI QIBs for specific clinical endpoints [7,8,12]. Quantitative analysis of mpMRI data estimates parameters characterizing underlying tumor physiology. All major MRI vendors have tools for DCE MRI semi-quantitative analysis or Standard Tofts (e.g., NordicICE; Nordic Neuro Lab, Bergen, Norway). Currently, a selection of open-source tools exists for time-course compartmental models or basic Tofts analysis of DCE data (e.g., Madym [22], MITK-ModelFit [55], FireVoxel (<https://firevoxel.org/>, accessed on 10 October 2023), DCENET [56]). DW MRI tools for monoexponential ADC modeling are widely available on all major MRI vendor platforms. Many cutting-edge advanced analysis routines for bi-exponential or kurtosis imaging from other providers are still closed source, based on in-house code, limiting wider adoption [25]. Few tools offer a one-stop shop for multiple modalities. One comparable example is the C++-based Madym software (v4.15.2), which can analyze DCE, DWI (ADC, IVIM), and relaxometry (T_1 and T_2 mapping) [22], but does not have OMM or verification status offered by NCI/QIN Benchmarking. OMM is provided by the ROCKETSHIP platform [23] for DCE models, but there is no other similar offering for DW MRI.

QAMPER is currently available through a material transfer agreement (MTA) with our center. Our group has experience with MR Fingerprinting (MRF) (refs: phantom, brain metastases [57,58]), which provides simultaneous T_1 and T_2 relaxometry measures in a clinically feasible amount of time. We plan to include the MRF reconstruction algorithm in our next implementation of the QAMPER platform. In the future, we plan to make MRI-QAMPER available via cloud architecture (Figure 4) [59].

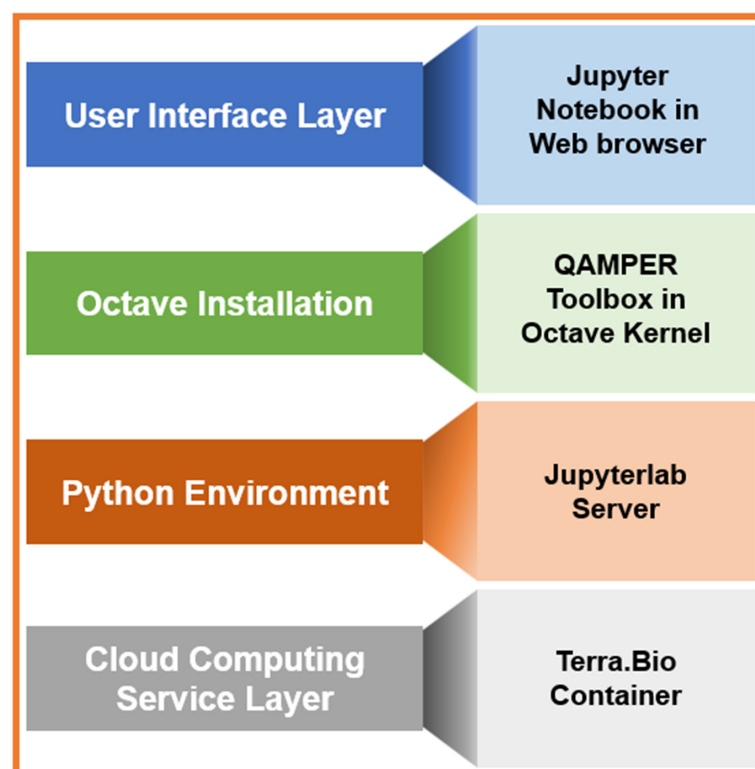


Figure 4. Proposed architecture schema for cloud implementation of MRI-QAMPER.

5. Conclusions

Given the need to develop quantitative tools estimating robust imaging biomarkers for clinical applications in oncology, MRI-QAMPER (v3.0) is a standardized platform that can process mpMRI data seamlessly from the brain, head and neck, thyroid, prostate, pancreas, and bladder. Output of MRI-QAMPER routines has been validated using RSNA QIBA DROs for both DCE MRI (Barboriak Lab, Duke University) and DW MRI (Chenevert Lab, University of Michigan).

There are a number of platforms for quantitative MRI with either DCE and/or DW and/or MR relaxometry. QAMPER stands out due to its extensive features and vetting by NCI/QIN. In addition, none of the existing platforms have the non-Gaussian IVIM (NG-IVIM) DW MRI fitting routine in their packages, which was developed and implemented by our group [25].

ETM has been tested in the OSUPI Task Force DCE challenge (manuscript under review) to benchmark and progress K^{trans} calculation as a diagnostic or prognostic biomarker in brain metastasis. Other DCE pharmacokinetic models, such as SSM, CTUM, and 2CXM, need to be validated through DRO and CCPs. DW MRI routines have been thoroughly vetted through DRO and CCP events, including the multi-b value prostate diffusion imaging challenge for prostate cancer detection led by Dr. Pete LaViolette at Medical College Wisconsin (MCW) [20]. The software has been distributed to NCI QIN collaborators to perform inter-site data validation testing and is available upon request through material transfer agreements (MTA).

Author Contributions: Conceptualization, A.S.-D., E.L., R.P. and A.S.K.; methodology, A.S.-D., E.L., R.P. and A.S.K.; software, A.S.-D., E.L., R.P. and A.S.K.; validation, A.S.-D., E.L., R.P., A.S.K., P.S.L. and L.H.S.; formal analysis, A.S.-D., E.L., R.P., A.S.K., V.H., O.A. and A.C.G.; investigation, A.S.-D., E.L. and R.P.; resources, A.S.-D.; data curation, A.S.-D., E.L., R.P. and A.S.K.; writing—original draft preparation, A.S.-D., E.L., R.P., A.S.K., P.S.L., V.H., O.A., A.C.G., B.H.B., J.R., R.J.W., N.Y.L. and L.H.S.; writing—review and editing, A.S.-D., E.L., R.P., A.S.K., P.S.L., V.H., O.A., A.C.G., B.H.B., J.R., R.J.W., N.Y.L. and L.H.S.; visualization, A.S.-D., E.L., R.P. and A.S.K.; supervision, A.S.-D.; project administration, A.S.-D.; funding acquisition, A.S.-D. All authors have read and agreed to the published version of the manuscript.

Funding: This research was supported by U01 CA211205 and, in part, through the NIH/NCI Cancer Center Support Grant P30 CA008748.

Institutional Review Board Statement: The patient data in this study analyzed with MRI-QAMPER were acquired under multiple, organ-specific IRB protocols, which are detailed in the relevant citations [16–21].

Informed Consent Statement: Informed consent was obtained from all patients whose data were used in this study.

Data Availability Statement: The data presented in this study will be provided upon reasonable request.

Conflicts of Interest: The authors declare no conflict of interest.

Appendix A

DCE MRI pharmacokinetic analysis.

Appendix A.1. Precontrast T_{10} Fitting

A series of gradient-echo images are acquired using the variable flip angle (FA) method and fixed repetition time (TR) and echo time (TE). The signal intensity for the spoiled gradient recalled (SPGR) sequence is given by [31]

$$S(t) = \frac{M_0 \sin(\theta) e^{-\text{TE}R_2^*(t)} (1 - e^{-\text{TR}R_1(t)})}{(1 - \cos(\theta) e^{-\text{TR}R_1(t)})} \quad (\text{A1})$$

This can be written as follows to estimate pre-contrast longitudinal relaxation time, T_1 , and equilibrium magnetization, M_0 :

$$\frac{S(t)}{\sin(\theta)} = E_1 \frac{S(t)}{\tan(\theta)} + M_0(1 - E_1) \tag{A2}$$

where $E_1 = e^{-TRR_1(t)}$, $S(t)$ is the voxel signal intensity at time t , M_0 is the equilibrium magnetization of the protons, θ is the flip angle. Longitudinal relaxation rate $R_1(t)$ (where $R_1 = 1/T_1$) and transverse relaxation rate $R_2^*(t)$ (where $R_2^* = 1/T_2^*$) are the time courses of longitudinal and transverse relaxation rates, respectively, here, $e^{-TER_2^*(t)} \approx 1$.

Appendix A.2. Signal-to-CA Concentration Calculation

The signal intensity in a voxel, measured from an SPGR T_1w sequence for a given FA expressed in Equation (A1) can be expressed for the time course of $R_1(t)$ as follows:

$$R_1(t) = \frac{1}{TR} \ln \left(\frac{1 - \left(\frac{S(t)\cos(\theta)}{M_0\sin(\theta)} \right)}{1 - \left(\frac{S(t)}{M_0\sin(\theta)} \right)} \right) \tag{A3}$$

In the limit of fast water exchange, the change in water proton relaxation rate, ΔR_1 , (i.e., $\Delta R_1(t) = (R_1(t) - R_{10}) [s^{-1}]$) due to CA relaxivity, $r_1 [(\text{mM})^{-1}\text{s}^{-1}]$, is linearly related to the tissue CA concentration, C_t (mM),

$$R_1(t) = R_{10} + r_1 C_t(t) \rightarrow \Delta R_1(t) = r_1 C_t(t) \tag{A4}$$

where R_{10} is the pre-contrast longitudinal relaxation rate.

Appendix A.3. Compartmental Tissue Uptake Model (CTUM)

This model assumes no back flux of CA from the interstitium to the plasma compartment; thus, v_e is not measurable. Three parameters, v_p , F_p , and $K^{\text{trans}} = E \times F_p$, can be estimated using:

$$C_t(t) = C_p \otimes F_p(t) (e^{-\frac{t}{T_p}} + E(1 - e^{-\frac{t}{T_p}})) \tag{A5}$$

where E is the first extraction fraction, $E = PS / ((F_p + PS))$, and T_p is the mean plasma transit time, F_p is the blood plasma perfusion, and PS is the capillary permeability surface area product [5].

Appendix A.4. Two-Compartment Exchange Model (2CXM)

The 2CXM estimates F_p , PS , v_p , and v_e [5].

$$C_t(t) = C_p \times A \otimes F_p(t) \tag{A6}$$

where A is given by,

$$A(t) = e^{-tB_+} + E_- (e^{-tB_-} - e^{-tB_+}) \tag{A7}$$

and B_{\pm} is given by

$$B_{\pm} = \frac{1}{2} \left(T_p^{-1} + T_E^{-1} \pm \sqrt{(T_p^{-1} + T_E^{-1})^2 - 4T_E^{-1}T_B^{-1}} \right) \tag{A8}$$

$$E_- = \frac{B_+ - T_B^{-1}}{B_+ - B_-}, \tag{A9}$$

$$T_p = \frac{v_p}{PS + F_p}; T_E = \frac{v_e}{PS}; T_B = \frac{v_p}{F_p} \tag{A10}$$

References

1. Grover, V.P.; Tognarelli, J.M.; Crossey, M.M.; Cox, I.J.; Taylor-Robinson, S.D.; McPhail, M.J. Magnetic Resonance Imaging: Principles and Techniques: Lessons for Clinicians. *J. Clin. Exp. Hepatol.* **2015**, *5*, 246–255. [[CrossRef](#)] [[PubMed](#)]
2. Kabasawa, H. MR Imaging in the 21st Century: Technical Innovation over the First Two Decades. *Magn. Reson. Med. Sci.* **2022**, *21*, 71–82. [[CrossRef](#)] [[PubMed](#)]
3. Chalavi, S.; Simmons, A.; Dijkstra, H.; Barker, G.J.; Reinders, A.A.T.S. Quantitative and qualitative assessment of structural magnetic resonance imaging data in a two-center study. *BMC Med. Imaging* **2012**, *12*, 27. [[CrossRef](#)] [[PubMed](#)]
4. Konar, A.S.; Paudyal, R.; Shah, A.D.; Fung, M.; Banerjee, S.; Dave, A.; Lee, N.; Hatzoglou, V.; Shukla-Dave, A. Qualitative and quantitative performance of magnetic resonance image compilation (MAGiC) method: An exploratory analysis for head and neck imaging. *Cancers* **2022**, *14*, 3624. [[CrossRef](#)] [[PubMed](#)]
5. Sourbron, S.P.; Buckley, D.L. On the scope and interpretation of the Tofts models for DCE-MRI. *Magn. Reson. Med.* **2011**, *66*, 735–745. [[CrossRef](#)]
6. Chawla, S.; Kim, S.; Wang, S.; Poptani, H. Diffusion-weighted imaging in head and neck cancers. *Future Oncol.* **2009**, *5*, 959–975. [[CrossRef](#)] [[PubMed](#)]
7. Keenan, K.E.; Biller, J.R.; Delfino, J.G.; Boss, M.A.; Does, M.D.; Evelhoch, J.L.; Griswold, M.A.; Gunter, J.L.; Hinks, R.S.; Hoffman, S.W.; et al. Recommendations towards standards for quantitative MRI (qMRI) and outstanding needs. *J. Magn. Reson. Imaging* **2019**, *49*, e26–e39. [[CrossRef](#)]
8. Shukla-Dave, A.; Obuchowski, N.A.; Chenevert, T.L.; Jambawalikar, S.; Schwartz, L.H.; Malyarenko, D.; Huang, W.; Noworolski, S.M.; Young, R.J.; Shiroishi, M.S.; et al. Quantitative imaging biomarkers alliance (QIBA) recommendations for improved precision of DWI and DCE-MRI derived biomarkers in multicenter oncology trials. *J. Magn. Reson. Imaging* **2019**, *49*, e101–e121. [[CrossRef](#)]
9. Padhani, A.R.; Khan, A.A. Diffusion-weighted (DW) and dynamic contrast-enhanced (DCE) magnetic resonance imaging (MRI) for monitoring anticancer therapy. *Target. Oncol.* **2010**, *5*, 39–52. [[CrossRef](#)]
10. Riaz, N.; Sherman, E.; Pei, X.; Schöder, H.; Grkovski, M.; Paudyal, R.; Katabi, N.; Selenica, P.; Yamaguchi, T.N.; Ma, D.; et al. Precision Radiotherapy: Reduction in Radiation for Oropharyngeal Cancer in the 30 ROC Trial. *J. Natl. Cancer Inst.* **2021**, *113*, 742–751. [[CrossRef](#)]
11. Winfield, J.M.; Payne, G.S.; Weller, A.; deSouza, N.M. DCE-MRI, DW-MRI, and MRS in Cancer: Challenges and Advantages of Implementing Qualitative and Quantitative Multi-parametric Imaging in the Clinic. *Top. Magn. Reson. Imaging* **2016**, *25*, 245–254. [[CrossRef](#)] [[PubMed](#)]
12. Farahani, K.; Tata, D.; Nordstrom, R.J. QIN Benchmarks for Clinical Translation of Quantitative Imaging Tools. *Tomography* **2019**, *5*, 1–6. [[CrossRef](#)] [[PubMed](#)]
13. Obuchowski, N.A.; Reeves, A.P.; Huang, E.P.; Wang, X.F.; Buckler, A.J.; Kim, H.J.; Barnhart, H.X.; Jackson, E.F.; Giger, M.L.; Pennello, G.; et al. Quantitative imaging biomarkers: A review of statistical methods for computer algorithm comparisons. *Stat. Methods Med. Res.* **2015**, *24*, 68–106. [[CrossRef](#)] [[PubMed](#)]
14. Barboriak, D. QIBA DRO for DCE MRI. 2018.
15. Kurland, B.F.; Gerstner, E.R.; Mountz, J.M.; Schwartz, L.H.; Ryan, C.W.; Graham, M.M.; Buatti, J.M.; Fennessy, F.M.; Eikman, E.A.; Kumar, V.; et al. Promise and pitfalls of quantitative imaging in oncology clinical trials. *Magn. Reson. Imaging* **2012**, *30*, 1301–1312. [[CrossRef](#)] [[PubMed](#)]
16. Shah, A.D.; Shridhar Konar, A.; Paudyal, R.; Oh, J.H.; LoCastro, E.; Nuñez, D.A.; Swinburne, N.; Vachha, B.; Ulaner, G.A.; Young, R.J.; et al. Diffusion and Perfusion MRI Predicts Response Preceding and Shortly After Radiosurgery to Brain Metastases: A Pilot Study. *J. Neuroimaging* **2021**, *31*, 317–323. [[CrossRef](#)] [[PubMed](#)]
17. Paudyal, R.; Oh, J.H.; Riaz, N.; Venigalla, P.; Li, J.; Hatzoglou, V.; Leeman, J.; Nunez, D.A.; Lu, Y.; Deasy, J.O.; et al. Intravoxel incoherent motion diffusion-weighted MRI during chemoradiation therapy to characterize and monitor treatment response in human papillomavirus head and neck squamous cell carcinoma. *J. Magn. Reson. Imaging* **2017**, *45*, 1013–1023. [[CrossRef](#)] [[PubMed](#)]
18. Nunez, D.A.; Lu, Y.; Paudyal, R.; Hatzoglou, V.; Moreira, A.L.; Oh, J.H.; Stambuk, H.E.; Mazaheri, Y.; Gonen, M.; Ghossein, R.A.; et al. Quantitative Non-Gaussian Intravoxel Incoherent Motion Diffusion-Weighted Imaging Metrics and Surgical Pathology for Stratifying Tumor Aggressiveness in Papillary Thyroid Carcinomas. *Tomography* **2019**, *5*, 26–35. [[CrossRef](#)]
19. Paudyal, R.; Lu, Y.; Hatzoglou, V.; Moreira, A.; Stambuk, H.E.; Oh, J.H.; Cunanan, K.M.; Aramburu Nunez, D.; Mazaheri, Y.; Gonen, M.; et al. Dynamic contrast-enhanced MRI model selection for predicting tumor aggressiveness in papillary thyroid cancers. *NMR Biomed.* **2020**, *33*, e4166. [[CrossRef](#)]
20. McGarry, S.D.; Brehler, M.; Bukowy, J.D.; Lowman, A.K.; Bobholz, S.A.; Duenweg, S.R.; Banerjee, A.; Hurrell, S.L.; Malyarenko, D.; Chenevert, T.L.; et al. Multi-Site Concordance of Diffusion-Weighted Imaging Quantification for Assessing Prostate Cancer Aggressiveness. *J. Magn. Reson. Imaging* **2022**, *55*, 1745–1758. [[CrossRef](#)]
21. Kinh Do, R.; Reingold, M.; Paudyal, R.; Oh, J.H.; Konar, A.S.; LoCastro, E.; Goodman, K.A.; Shukla-Dave, A. Diffusion-Weighted and Dynamic Contrast-Enhanced MRI Derived Imaging Metrics for Stereotactic Body Radiotherapy of Pancreatic Ductal Adenocarcinoma: Preliminary Findings. *Tomography* **2020**, *6*, 261–271. [[CrossRef](#)]
22. Berks, M.; Parker, G.; Little, R.; Cheung, S. Madym: A C++ toolkit for quantitative DCE-MRI analysis. *J. Open Source Softw.* **2021**, *6*, 3523. [[CrossRef](#)]

23. Barnes, S.R.; Ng, T.S.; Santa-Maria, N.; Montagne, A.; Zlokovic, B.V.; Jacobs, R.E. ROCKETSHIP: A flexible and modular software tool for the planning, processing and analysis of dynamic MRI studies. *BMC Med. Imaging* **2015**, *15*, 19. [[CrossRef](#)]
24. Ewing, J.R.; Bagher-Ebadian, H. Model selection in measures of vascular parameters using dynamic contrast-enhanced MRI: Experimental and clinical applications. *NMR Biomed.* **2013**, *26*, 1028–1041. [[CrossRef](#)] [[PubMed](#)]
25. Lu, Y.; Jansen, J.F.; Mazaheri, Y.; Stambuk, H.E.; Koutcher, J.A.; Shukla-Dave, A. Extension of the intravoxel incoherent motion model to non-gaussian diffusion in head and neck cancer. *J. Magn. Reson. Imaging* **2012**, *36*, 1088–1096. [[CrossRef](#)] [[PubMed](#)]
26. Li, X.; Morgan, P.S.; Ashburner, J.; Smith, J.; Rorden, C. The first step for neuroimaging data analysis: DICOM to NIfTI conversion. *J. Neurosci. Methods* **2016**, *264*, 47–56. [[CrossRef](#)]
27. Yushkevich, P.A.; Gao, Y.; Gerig, G. ITK-SNAP: An interactive tool for semi-automatic segmentation of multi-modality biomedical images. In Proceedings of the 2016 38th Annual International Conference of the IEEE Engineering in Medicine and Biology Society (EMBC), Orlando, FL, USA, 16–20 August 2016; pp. 3342–3345.
28. Tofts, P.S.; Brix, G.; Buckley, D.L.; Evelhoch, J.L.; Henderson, E.; Knopp, M.V.; Larsson, H.B.; Lee, T.Y.; Mayr, N.A.; Parker, G.J.; et al. Estimating kinetic parameters from dynamic contrast-enhanced T(1)-weighted MRI of a diffusable tracer: Standardized quantities and symbols. *J. Magn. Reson. Imaging* **1999**, *10*, 223–232. [[CrossRef](#)]
29. Le Bihan, D. Intravoxel incoherent motion imaging using steady-state free precession. *Magn. Reson. Med.* **1988**, *7*, 346–351. [[CrossRef](#)]
30. Jensen, J.H.; Helpert, J.A.; Ramani, A.; Lu, H.; Kaczynski, K. Diffusional kurtosis imaging: The quantification of non-gaussian water diffusion by means of magnetic resonance imaging. *Magn. Reson. Med.* **2005**, *53*, 1432–1440. [[CrossRef](#)]
31. Bagher-Ebadian, H.; Jain, R.; Nejad-Davarani, S.P.; Mikkelsen, T.; Lu, M.; Jiang, Q.; Scarpace, L.; Arbab, A.S.; Narang, J.; Soltanian-Zadeh, H.; et al. Model selection for DCE-T1 studies in glioblastoma. *Magn. Reson. Med.* **2012**, *68*, 241–251. [[CrossRef](#)]
32. Deoni, S.C.; Peters, T.M.; Rutt, B.K. High-resolution T1 and T2 mapping of the brain in a clinically acceptable time with DESPOT1 and DESPOT2. *Magn. Reson. Med.* **2005**, *53*, 237–241. [[CrossRef](#)]
33. Patlak, C.S.; Blasberg, R.G.; Fenstermacher, J.D. Graphical evaluation of blood-to-brain transfer constants from multiple-time uptake data. *J. Cereb. Blood Flow. Metab.* **1983**, *3*, 1–7. [[CrossRef](#)] [[PubMed](#)]
34. Landis, C.S.; Li, X.; Telang, F.W.; Coderre, J.A.; Micca, P.L.; Rooney, W.D.; Latour, L.L.; Véték, G.; Pályka, I.; Springer, C.S., Jr. Determination of the MRI contrast agent concentration time course in vivo following bolus injection: Effect of equilibrium transcytolemmal water exchange. *Magn. Reson. Med.* **2000**, *44*, 563–574. [[CrossRef](#)] [[PubMed](#)]
35. Li, X.; Rooney, W.D.; Springer, C.S., Jr. A unified magnetic resonance imaging pharmacokinetic theory: Intravascular and extracellular contrast reagents. *Magn. Reson. Med.* **2005**, *54*, 1351–1359. [[CrossRef](#)]
36. Paudyal, R.; Poptani, H.; Cai, K.; Zhou, R.; Glickson, J.D. Impact of transvascular and cellular-interstitial water exchange on dynamic contrast-enhanced magnetic resonance imaging estimates of blood to tissue transfer constant and blood plasma volume. *J. Magn. Reson. Imaging* **2013**, *37*, 435–444. [[CrossRef](#)]
37. Shukla-Dave, A.; Lee, N.; Stambuk, H.; Wang, Y.; Huang, W.; Thaler, H.T.; Patel, S.G.; Shah, J.P.; Koutcher, J.A. Average arterial input function for quantitative dynamic contrast enhanced magnetic resonance imaging of neck nodal metastases. *BMC Med. Phys.* **2009**, *9*, 4. [[CrossRef](#)]
38. Li, X.; Welch, E.B.; Chakravarthy, A.B.; Mayer, I.; Kelley, M.; Meszoely, I.; Means-Powell, J.; Gore, J.C.; Yankeelov, T.E. A semi-automated method for obtaining the arterial input function in dynamic breast data. *Proc. Intl. Soc. Mag. Reson. Med. (ISMRM)* **2010**, *18*, 2729.
39. Chenevert, T.L.; McKeever, P.E.; Ross, B.D. Monitoring early response of experimental brain tumors to therapy using diffusion magnetic resonance imaging. *Clin. Cancer Res. Off. J. Am. Assoc. Cancer Res.* **1997**, *3*, 1457–1466.
40. Cheng, H.L.; Stikov, N.; Ghugre, N.R.; Wright, G.A. Practical medical applications of quantitative MR relaxometry. *J. Magn. Reson. Imaging* **2012**, *36*, 805–824. [[CrossRef](#)]
41. Wansapura, J.P.; Holland, S.K.; Dunn, R.S.; Ball, W.S., Jr. NMR relaxation times in the human brain at 3.0 tesla. *J. Magn. Reson. Imaging* **1999**, *9*, 531–538. [[CrossRef](#)]
42. Gelman, N.; Gorell, J.M.; Barker, P.B.; Savage, R.M.; Spickler, E.M.; Windham, J.P.; Knight, R.A. MR imaging of human brain at 3.0 T: Preliminary report on transverse relaxation rates and relation to estimated iron content. *Radiology* **1999**, *210*, 759–767. [[CrossRef](#)]
43. Gelman, N.; Ewing, J.R.; Gorell, J.M.; Spickler, E.M.; Solomon, E.G. Interregional variation of longitudinal relaxation rates in human brain at 3.0 T: Relation to estimated iron and water contents. *Magn. Reson. Med.* **2001**, *45*, 71–79. [[CrossRef](#)] [[PubMed](#)]
44. Fatemi, Y.; Danyali, H.; Helfroush, M.S.; Amiri, H. Fast T(2) mapping using multi-echo spin-echo MRI: A linear order approach. *Magn. Reson. Med.* **2020**, *84*, 2815–2830. [[CrossRef](#)] [[PubMed](#)]
45. Liao, Y.P.; Urayama, S.I.; Isa, T.; Fukuyama, H. Optimal Model Mapping for Intravoxel Incoherent Motion MRI. *Front. Hum. Neurosci.* **2021**, *15*, 617152. [[CrossRef](#)] [[PubMed](#)]
46. Ewing, J.R.; Brown, S.L.; Lu, M.; Panda, S.; Ding, G.; Knight, R.A.; Cao, Y.; Jiang, Q.; Nagaraja, T.N.; Churchman, J.L.; et al. Model selection in magnetic resonance imaging measurements of vascular permeability: Gadomer in a 9L model of rat cerebral tumor. *J. Cereb. Blood Flow. Metab.* **2006**, *26*, 310–320. [[CrossRef](#)]
47. Kim, S.; Quon, H.; Loevner, L.A.; Rosen, M.A.; Dougherty, L.; Kilger, A.M.; Glickson, J.D.; Poptani, H. Transcytolemmal water exchange in pharmacokinetic analysis of dynamic contrast-enhanced MRI data in squamous cell carcinoma of the head and neck. *J. Magn. Reson. Imaging Off. J. Int. Soc. Magn. Reson. Med.* **2007**, *26*, 1607–1617. [[CrossRef](#)]

48. Akaike, H. A new look at the statistical model identification. *IEEE Trans. Autom. Control* **1974**, *19*, 716–723. [[CrossRef](#)]
49. Banerji, A.; Naish, J.H.; Watson, Y.; Jayson, G.C.; Buonaccorsi, G.A.; Parker, G.J. DCE-MRI model selection for investigating disruption of microvascular function in livers with metastatic disease. *J. Magn. Reson. Imaging* **2012**, *35*, 196–203. [[CrossRef](#)]
50. Luybaert, R.; Ingrisich, M.; Sourbron, S.; De Mey, J. The Akaike information criterion in DCE-MRI: Does it improve the haemodynamic parameter estimates? *Phys. Med. Biol.* **2012**, *57*, 3609. [[CrossRef](#)]
51. Schwarz, G. Estimating the dimension of a model. *Ann. Stat.* **1978**, *6*, 461–464. [[CrossRef](#)]
52. Ger, R.B.; Mohamed, A.S.R.; Awan, M.J.; Ding, Y.; Li, K.; Fave, X.J.; Beers, A.L.; Driscoll, B.; Elhalawani, H.; Hormuth, D.A.; et al. A Multi-Institutional Comparison of Dynamic Contrast-Enhanced Magnetic Resonance Imaging Parameter Calculations. *Sci. Rep.* **2017**, *7*, 11185. [[CrossRef](#)]
53. Malyarenko, D.; Pang, Y.; Amouzandeh, G.; Chenevert, T. *Numerical DWI Phantoms to Optimize Accuracy and Precision of Quantitative Parametric Maps for Non-Gaussian Diffusion*; SPIE: Bellingham, DC, USA, 2020; Volume 11313.
54. Harrington, K.A.; Shukla-Dave, A.; Paudyal, R.; Do, R.K.G. MRI of the Pancreas. *J. Magn. Reson. Imaging* **2021**, *53*, 347–359. [[CrossRef](#)] [[PubMed](#)]
55. Debus, C.; Floca, R.; Ingrisich, M.; Kompan, I.; Maier-Hein, K.; Abdollahi, A.; Nolden, M. MITK-ModelFit: A generic open-source framework for model fits and their exploration in medical imaging—design, implementation and application on the example of DCE-MRI. *BMC Bioinform.* **2019**, *20*, 31. [[CrossRef](#)] [[PubMed](#)]
56. Liu, J.; Shao, L.; Zhou, C.; Yan, Z.; Han, Y.; Song, Y. DCE-Net: A Dynamic Context Encoder Network for Liver Tumor Segmentation. 2023. Available online: <https://www.researchsquare.com/article/rs-2272616/v1> (accessed on 10 October 2023).
57. Shridhar Konar, A.; Qian, E.; Geethanath, S.; Buonincontri, G.; Obuchowski, N.A.; Fung, M.; Gomez, P.; Schulte, R.; Cencini, M.; Tosetti, M.; et al. Quantitative imaging metrics derived from magnetic resonance fingerprinting using ISMRM/NIST MRI system phantom: An international multicenter repeatability and reproducibility study. *Med. Phys.* **2021**, *48*, 2438–2447. [[CrossRef](#)] [[PubMed](#)]
58. Konar, A.S.; Shah, A.D.; Paudyal, R.; Fung, M.; Banerjee, S.; Dave, A.; Hatzoglou, V.; Shukla-Dave, A. Quantitative Relaxometry Metrics for Brain Metastases Compared to Normal Tissues: A Pilot MR Fingerprinting Study. *Cancers* **2022**, *14*, 5606. [[CrossRef](#)] [[PubMed](#)]
59. Apte, A.P.; LoCastro, E.; Iyer, A.; Jiang, J.; Oh, J.H.; Veeraraghavan, H.; Shukla-Dave, A.; Deasy, J.O. Technical Note: STRATIS: A Cloud-enabled Software Toolbox for Radiotherapy and Imaging Analysis. *bioRxiv* **2022**. [[CrossRef](#)]

Disclaimer/Publisher’s Note: The statements, opinions and data contained in all publications are solely those of the individual author(s) and contributor(s) and not of MDPI and/or the editor(s). MDPI and/or the editor(s) disclaim responsibility for any injury to people or property resulting from any ideas, methods, instructions or products referred to in the content.